



## OPEN ACCESS

## EDITED BY

Sandeep Kumar,  
Deemed to be University, India

## REVIEWED BY

Selvakumar Palanisamy,  
Khalifa University, United Arab Emirates  
Urmila Chakraborty,  
Indian Institute of Technology Delhi, India

## \*CORRESPONDENCE

Riccarda Antiochia,  
✉ riccarda.antiochia@uniroma1.it

RECEIVED 14 November 2024

ACCEPTED 19 February 2025

PUBLISHED 27 March 2025

## CITATION

Tortolini C, Barbagallo F, Passeri D, Marrani AG, Isidori AM, Gianfrilli D and Antiochia R (2025) An ecofriendly AuNPs/semi-amorphous MOF-based sensor for *in-situ* testosterone monitoring for clinical diagnosis and doping control.  
*Front. Sens.* 6:1527587.  
doi: 10.3389/fsens.2025.1527587

## COPYRIGHT

© 2025 Tortolini, Barbagallo, Passeri, Marrani, Isidori, Gianfrilli and Antiochia. This is an open-access article distributed under the terms of the [Creative Commons Attribution License \(CC BY\)](https://creativecommons.org/licenses/by/4.0/). The use, distribution or reproduction in other forums is permitted, provided the original author(s) and the copyright owner(s) are credited and that the original publication in this journal is cited, in accordance with accepted academic practice. No use, distribution or reproduction is permitted which does not comply with these terms.

# An ecofriendly AuNPs/semi-amorphous MOF-based sensor for *in-situ* testosterone monitoring for clinical diagnosis and doping control

Cristina Tortolini<sup>1</sup>, Federica Barbagallo<sup>2</sup>, Daniele Passeri<sup>3</sup>, Andrea Giacomo Marrani<sup>4</sup>, Andrea M. Isidori<sup>1</sup>, Daniele Gianfrilli<sup>1</sup> and Riccarda Antiochia<sup>5\*</sup>

<sup>1</sup>Department of Experimental Medicine, Sapienza University of Rome, Rome, Italy, <sup>2</sup>Department of Medicine and Surgery, "Kore" University of Enna, Enna, Italy, <sup>3</sup>Department of Basic and Applied Sciences for Engineering, Sapienza University of Rome, Rome, Italy, <sup>4</sup>Department of Chemistry, Sapienza University of Rome, Rome, Italy, <sup>5</sup>Department of Chemistry and Drug Technologies, Sapienza University of Rome, Rome, Italy

A novel ecofriendly electrochemical sensor for *in-situ* detection of testosterone based on gold nanoparticles (AuNPs) and a semi-amorphous metal organic framework (MOF) has been developed for clinical diagnosis and doping control. For this purpose, MIL-100(Fe) has been synthesized according to a green path with crystallization times tuned in the range 2–24 h. The sensor platform was constructed via drop-casting MOF and AuNPs onto a graphene (GPH) screen-printed electrode (SPE) surface. The surface structure and morphology and the electrochemical properties of unmodified and modified electrodes were investigated by (SEM), energy-dispersive X-ray spectroscopy analysis (EDX), X-ray photoelectron spectroscopy (XPS), Raman spectroscopy, cyclic voltammetry (CV) and electrochemical impedance spectroscopy (EIS), demonstrating the enhanced electrochemical response of the platform modified with MOF obtained with the shorter crystallization time of 2 h (MOF2h) and AuNPs, compared to unmodified electrode. The AuNPs/MOF2h/GPH/SPE based sensor was responsive to nanomolar concentrations of testosterone, showing a wide linear range from 1 to 50 nM and a detection limit (LOD) of 0.5 nM, which correlates to the serum concentration values of healthy males. The combination of these results with the excellent performance maintained by the proposed sensor when interfaced with a miniaturized potentiostat (Sensit-Smart) directly connected to a smartphone, highlights the potential of this device towards *in-situ* electrochemical testosterone sensing, in particular for medical diagnosis and for doping control.

## KEYWORDS

metal-organic frameworks, gold nanoparticles, electrochemical sensor, testosterone, clinical diagnosis, doping control

## 1 Introduction

Testosterone (17 $\beta$ -hydroxyandrost-4-en-3-one) is the primary male sex hormone and an anabolic steroid. It is vital for athletic performance and plays a significant role in the development of masculine traits (Berglund et al., 2011, Luetjens and Weinbauer, 2012). In humans, it is mostly produced by the male testes and the female ovaries, with minor

amounts also coming from the adrenal glands in both sexes. This substance is essential for spermatogenesis, the growth and upkeep of male internal and external genitalia and secondary sex traits, and the regulation of libido in both sexes (Kumar et al., 2010; Yadav et al., 2014).

Normal testosterone plasma levels range between 10 and 35 nM and from 0.6 to 2.5 nM in adult males and females, respectively (Scovell et al., 2015; Mohamad et al., 2016; Yuki et al., 2013). Although testosterone is also used exogenously in treatments (typically in its esterified form), prolonged use of this hormone can have a number of negative effects (Alvarado, 2010). However, it is frequently used in illegal activities to enhance the performances of athletes (McBride et al., 2018; Bhasin et al., 2001).

Due to the potential health concerns and to its capacity to enhance performance, the World Anti-Doping Agency (WADA) prohibits the use of this substance (Barroso et al., 2008; Wang et al., 2022).

Therefore, a fast, accurate, low-cost and *in-situ* detection of testosterone is of extreme importance not only for clinical diagnosis but also for anti-doping agencies (Lu et al., 2023).

Traditionally, methods such as gas-liquid chromatography/mass spectrometry, HPLC, enzyme-linked immunosorbent assay, and, more recently, mass spectrometry, have been widely used to measure the testosterone level in biological matrices with excellent sensitivity and selectivity (Fourou et al., 2018; Kozak et al., 2022; Laczka et al., 2011). However, these techniques require highly skilled laboratory personnel, costly and sophisticated equipment, laborious sample pretreatments, which result in considerable delays between sample collection and outcomes. Among voltammetric techniques, adsorptive stripping voltammetry (AdSV) was successfully used for the reduction of testosterone either at a hanging mercury drop electrode (HMDE) (Hu et al., 1993) or by using a lead film electrode (Tyszczyk, 2008), a bismuth film electrode (Levent et al., 2015) or a pencil graphite electrode with copper nanoparticle (Bozdoğan, 2023). However, AdSV shows some drawbacks, such as mercury toxicity, the need of preconcentration step of the sample, and possibility of adsorption of matrix components on the electrode surface. On the other hand, electrochemical sensors and biosensors, thanks to their ease of use, speed, accuracy, sensitivity, cost-effectiveness, portability, and possibility of miniaturization, have become popular point-of-care diagnostic devices (Liu et al., 2023; Ma et al., 2023; Xu et al., 2022). The goal of recent research in literature is to improve the electrochemical sensor's sensitivity by the arrangement and modification of the electrode surface (Yadav et al., 2013).

Several nanostructures have been employed for testosterone sensing, such as carbon nanotubes (Alam et al., 2021), nanosheets, metallic nanoparticles (Kozak et al., 2022; Bozdoğan, 2023), graphene oxide (Heidarimoghadam et al., 2016; Huang and Feng, 2024), molecularly-imprinted polymers (Sanchez-Almirola et al., 2023) and a number of strategies have been investigated to better modify the electrode surface in order to obtain larger surface area, enhanced conductivity, good biocompatibility and improved catalytic properties (Bahrami et al., 2021).

Metal-organic frameworks (MOFs) are a new class of multifunctional porous organic-inorganic compounds characterized by a cage-like structure consisting of metal ions and organic ligands (Delpiano et al., 2021). In recent years, thousands of MOFs have been described for potential applications in catalysis, (Jiao et al., 2018), (bio)

sensing (Mehmandoust et al., 2022; Dolgoplova et al., 2018), adsorption (Ayati et al., 2016; Jiang et al., 2019), gas storage (Ghanbari et al., 2020), enzyme carrier (Naseri et al., 2018; Wang and Liao, 2021) and drug delivery (Li et al., 2017; Roth Stefaniak et al., 2018; Mallakpour et al., 2022). The use of octahedral trivalent metals like iron, which have low toxicity and high biocompatibility, and the simplest aromatic carboxylates, such as trimesate, has been reported to create MOFs with excellent stability and hierarchical mesopores. One of the most popular Fe-based MOF is MIL-100(Fe), prepared by a combination of trimesic acid, as organic linker, and a Fe(II) salt.

It is one of the highest porous MOFs available, with two mesoporous cages with different diameters (2.5 nm and 2.9 nm), accessible through microporous windows (0.86 nm and 0.47–0.55 nm). In order to enhance its conductivity, in this work a film of AuNPs has been drop-casted onto the MOF structure resulting in improved sensitivity, thanks to a larger surface area. At present, the biggest challenge in the MIL-100(Fe) synthesis is to yield highly crystalline MOF under mild conditions, avoiding the use of toxic reagents, such as HF, HNO<sub>3</sub>, high temperature and pressure, which are normally used in the synthesis methods reported in literature.

In our work, we present a novel electrochemical sensor based on a disposable graphene SPE modified by a ecofriendly Fe-MOF and AuNPs for sensitive testosterone monitoring. The MOF synthesis time has been tuned from 2 to 24 h in order to investigate the correlation between longer synthesis times and enhanced electrochemical performances. ii) The electrode modification was carried out by two drop-casting steps: i) MOF; ii) AuNPs. The novelty of the work is based on two main issues: i) a total "green" synthesis process without the use of any harsh reagents; ii) a very short synthesis time (2 h) which allows the formation of a semi-amorphous MOF with improved electrochemical performances. AuNPs. Step-wise modification of the SPE surface and the changes in electron transfer characteristics were monitored by cyclic voltammetry (CV), and electrochemical impedance spectroscopy (EIS). Also, structural and morphological characterizations were carried out by scanning electron microscopy (SEM), energy-dispersive X-ray spectroscopy analysis (EDX), X-ray photoelectron spectroscopy (XPS) and Raman spectroscopy.

The performance of the developed sensor was finally tested on real human serum samples spiked with synthetic testosterone and the results compared to those obtained with a portable potentiostat, used to perform POC sensing, needed for the development of personalized medicine and for doping controls.

## 2 Materials and methods

### 2.1 Reagents and instrumentations

Testosterone ( $\geq 99\%$ , TST), sodium monobasic phosphate (Na<sub>2</sub>HPO<sub>4</sub>), sodium dibasic phosphate (NaH<sub>2</sub>PO<sub>4</sub>), potassium chloride (KCl), potassium ferricyanide (III) (K<sub>3</sub>[Fe(CN)<sub>6</sub>]), potassium ferrocyanide (II) (K<sub>4</sub>[Fe(CN)<sub>6</sub>]), trimesic acid (95%, H3BTC), iron (II) chloride tetrahydrate (99%, FeCl<sub>2</sub> · 4H<sub>2</sub>O), acetonitrile, tetraethylammonium tetrafluoro-borate ( $\geq 99\%$ ) and ethanol absolute (EtOH) were obtained from Sigma-Aldrich (Buchs, Switzerland). The gold nanoparticles (AuNPs, diameter 18–20 nm, 0.418 mg mL<sup>-1</sup>) were synthesized according to a procedure reported in our previous work (Tortolini et al., 2024a).

The morphology and the chemical composition of bare and modified electrodes were investigated by Scanning Electron Microscopy (SEM) and by Energy-Dispersive X-ray spectroscopy (EDX), respectively. The SEM/EDX measurements were performed with High-Resolution Field Emission Scanning Electron Microscopy (HR FESEM, Zeiss Auriga Microscopy, Jena, Germany).

XPS measurements were carried out using an Omicron NanoTechnology Multiprobe XPS system equipped with a Mg K $\alpha$  ( $h\nu = 1253.6$  eV) X-ray source. Ethanolic solutions of the MIL-100 (Fe) samples synthesized for 2 h and 24 h were drop casted onto hydrogenated Si wafers and let dry at room temperature. The samples were then mounted on the XPS sample holder with double-sided conductive scotch tape. The C 1s and Fe 2p photoionization regions were acquired using an analyzer pass energy of 20 eV and take-off angle of 21° with respect to the sample surface normal. The experimental spectra were theoretically reconstructed, fitting the secondary electrons' background to a Shirley function and the elastic peaks to pseudo-Voigt functions.

Raman spectra were run at room temperature in backscattering geometry with an inVia Renishaw micro-Raman spectrometer equipped with an air-cooled CCD detector and super-Notch filters. An Ar<sup>+</sup> ion laser ( $\lambda_{\text{laser}} = 514$  nm) was used, coupled to a Leica DLML microscope with a  $\times 20$  objective. The resolution was 2 cm<sup>-1</sup> and spectra were calibrated using the 520.5 cm<sup>-1</sup> line of a silicon wafer. Raman spectra were acquired in several different spots on the surface of the samples at 1% of laser power.

For Raman measurements, MOF samples, dispersed in ethanol, were drop-cast (about 100  $\mu\text{L}$ ) on silicon wafers and dried before performing the analyses.

All electrochemical characterizations involving cyclic voltammetry (CV) and electrochemical impedance spectroscopy (EIS) were performed using an Autolab Potentiostat/Galvanostat (Autolab PGSTAT204, Metrohm, Herisau, Switzerland) with the software Nova 1.1 v2.1.7. All measurements were carried out in a glass cell (model 6.1415.150, Metrohm, Herisau, Switzerland) with a conventional three-electrode configuration with an Ag/AgCl/KCl sat (198 mV vs. NHE) as a reference electrode (cat. 6.0726.100, Metrohm, Herisau, Switzerland), a glassy carbon rod as a counter electrode (cat. 6.1248.040, Metrohm, Herisau, Switzerland), a graphene screen-printed electrode (GPH/SPE, diameter 4 mm, 110 Metrohm, Herisau, Switzerland) and a classical glassy carbon electrode (GCE, diameter 2 mm, cat. 6.1204.600 GC Metrohm, Herisau, Switzerland) as working electrodes, respectively. All electrochemical measurements were carried out using three independent electrodes ( $n = 3$ ). The data were treated and analyzed using Sigma Plot software. The data were presented as mean  $\pm$  the standard deviation (SD).

For the smartphone-based sensing device experiments, a Sensit/SMART portable potentiostat (PalmSens, Houten, Netherlands) was used and directly connected to a smartphone for POC signal reading. All experiments were performed at room temperature (RT). pH measurements were made with a Metrohm pH meter model 780 (Switzerland).

## 2.2 Preparation of MIL-100(Fe)

The MIL-100(Fe) was synthesized according to a totally sustainable method already reported in literature (Sánchez-Sánchez et al., 2015; Guesh et al., 2017) and three samples were taken out from the reaction

mixture after 2 h, 12 h, and 24 h of vigorous stirring, named MOF2h and MOF24h, respectively (Scheme 1).

## 2.3 Fabrication of MOF/GPH/SPE and AuNPs/MOF/GPH/SPE

The MOF sensors were prepared using a bare graphene screen-printed electrode (GPH/SPE) modified by drop-casting 10  $\mu\text{L}$  of MOF solution of the three samples (MOF2 h, MOF12 h and MOF24 h), respectively.

Then the electrodes were dried under vacuum for 1 h at room temperature (RT). The AuNPs/MOF/GPH/SPEs were fabricated according to the previous procedure with a second drop-casting step of 10  $\mu\text{L}$  of AuNPs solution on the modified surfaces and letting dry at RT. All modified sensors were stored at RT until use.

## 2.4 Electrochemical procedures

The electrochemical measurements were performed by CV and EIS techniques. CV conditions were the followings: potential range:  $-0.2 - 0.7$  V and scan rate  $v = 0.025$  V s<sup>-1</sup>. For EIS analysis, the following parameters were employed: frequency range: 1–500 kHz, ac signal: 10 mV amplitude (0.2 V vs. Ag/AgCl). The solution used as redox probe was a mixture of 5 mM Fe(CN)<sub>6</sub><sup>3-/4-</sup> in 0.1 M KCl.

High-purity deionized water (resistance: 18.2 M $\Omega$  cm at 25°C; TOC <10  $\mu\text{g L}^{-1}$ ) obtained from Millipore (Molsheim, France) was used throughout experiments. All solutions were prepared in 0.1 M phosphate buffer, 0.1 M KCl, pH 7.0 (PBS).

Determination of the highest occupied and lowest unoccupied molecular orbital (HOMO and LUMO) energy states of AuNPs-MOF was carried out using acetonitrile (4 mL) containing 0.1 M tetraethylammonium tetrafluoroborate by scanning the potential in the range  $-1.45 - 1.55$  V, for 10 scans at 50 mV/s.

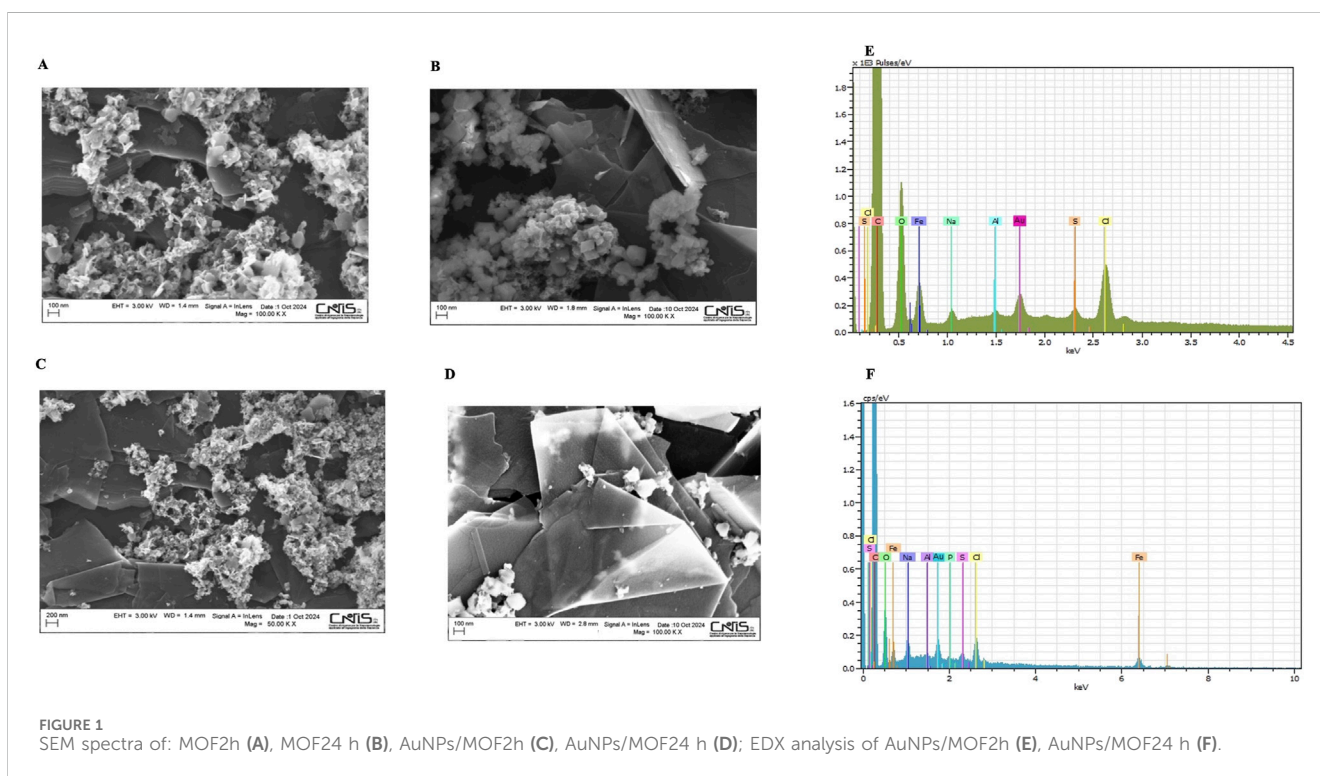
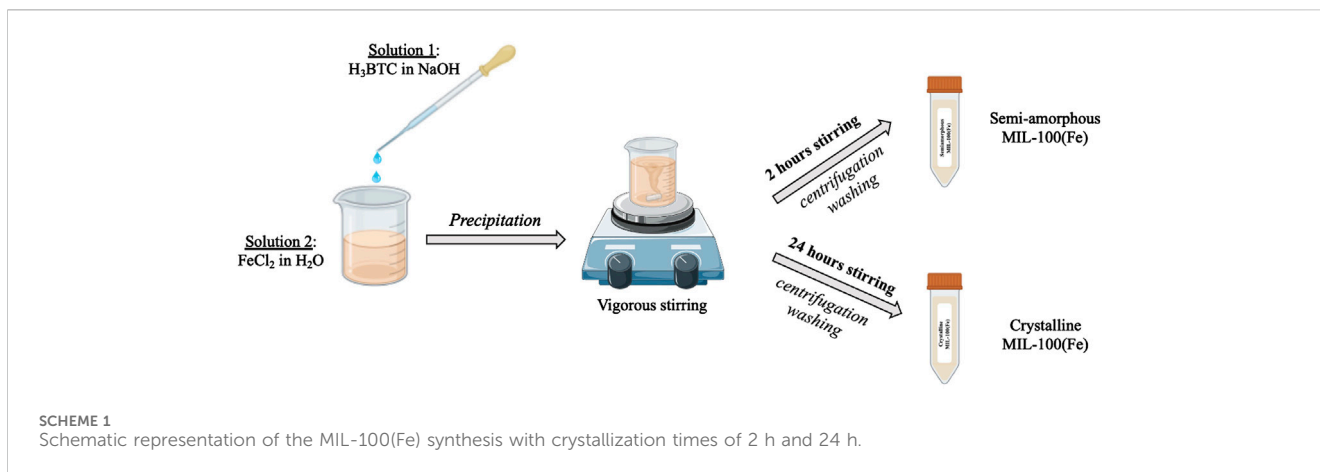
## 2.5 Preparation of real samples

Five serum samples were collected from healthy volunteers which had signed an informed consent before the study. The samples were stored at 4°C and were diluted 1:10 in 0.1 M PBS before electrochemical measurements. The standard addition method was applied to determine the added concentration of testosterone.

## 3 Results and discussion

### 3.1 Morphological and structural characterizations of modified electrodes

SEM images were carried out to investigate the surface morphology of modified electrodes. Figure 1 illustrates the MOF 2 h and 24 h, before and after the immobilization of AuNPs. It is clearly observed that, in the first case, most particles show an amorphous nature, attesting a low crystallinity of the material (Figure 1A), due to the reduced time of synthesis, whereas in the



second case (Figure 1B) well-defined crystals with octahedral shape, distinct facets and an average diameter of about 120 nm are clearly obtained. In order to certify the successful deposition of AuNPs on the MOF structures, SEM images were carried out after the drop-casting step of AuNPs on both electrodes. It is possible to see the presence of tiny scattered AuNPs, not uniformly distributed across the surface of the GPH/SPE in both cases (Figures 1C, D), suggesting a relatively favorable interaction between support and AuNPs. Figures 1E, F depicts the EDX elemental mapping images performed on the surfaces shown in Figure 1 (panels C and D), which confirm the presence of all fundamentals of MOF and AuNPs in the EDX spectra at both synthesis time, in particular the elemental peaks of carbon (C), oxygen (O), nitrogen (N), iron (Fe) and gold (Au), confirming the AuNPs/MOF nanostructure. SEM images of

bare GPH/SPE and AuNPs/GPH/SPE have been reported in Supplementary Figures S1A, B, for comparison.

PXRD experiments were performed in order to check the crystal structure of both MOFs (Figure not shown, as reported in our work under review). The MOF 24 h pattern perfectly matches with the simulated spectrum reported in literature for MIL-100(Fe). The agreement between both patterns is excellent, as every single peak of the simulated XRD pattern is present in the experimental XRD pattern with similar relative intensities without any other single detected XRD peak, leaving no doubts in the phase identification (Guesh et al., 2017; Han et al., 2017). Conversely, the MOF 2 h presents broad and less defined PXRD peaks, typical of the lack of long-range order features of amorphous materials. The dominant phase is still present, although it is also present a XRD peak found at  $9^{\circ}$ – $10^{\circ}$   $2\theta$ , which does not belong to the phase MIL-100(Fe), which

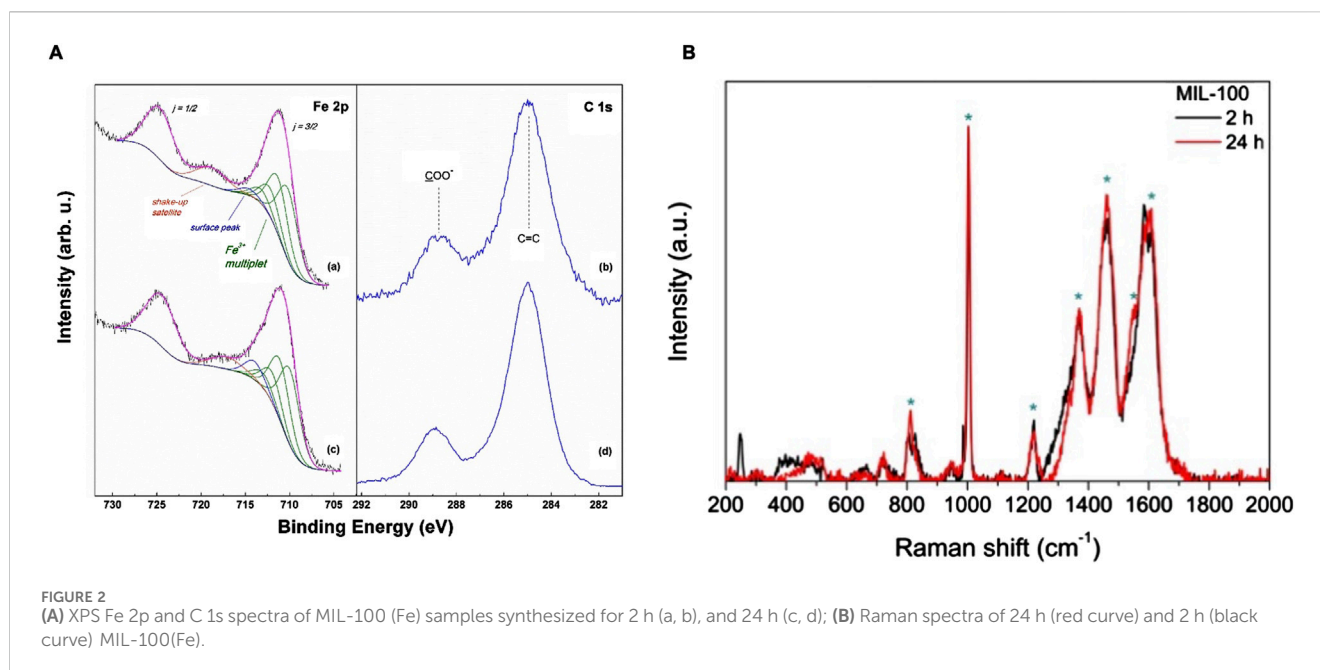


FIGURE 2 (A) XPS Fe 2p and C 1s spectra of MIL-100 (Fe) samples synthesized for 2 h (a, b), and 24 h (c, d); (B) Raman spectra of 24 h (red curve) and 2 h (black curve) MIL-100(Fe).

totally disappears at a prolonged synthesis time (24 h). XPS was used to ascertain the chemical composition of the MIL-100(Fe) samples taking advantage of the high sensitivity of photoelectron kinetic energies from the oxidation state and chemical environment. The Fe 2p ionization region (Figure 2A, a and c) is composed by a spin-orbit split doublet with components  $j = 3/2$  and  $5/2$  separated by a  $\Delta E_{SO} \sim 13.5$  eV. The two components are rather broad and the former displays a peak maximum at 711.3 eV. In order to evaluate in detail the oxidation state of Fe, the Fe 2p spectra were curve-fitted using the Gupta and Sen (GS) multiplets (Gupta and Sen, 1974; Gupta and Sen, 1975) theoretically predicted for high-spin  $Fe^{3+}$  ions and applied by Grosvenor et al. (2004); Biesinger et al. (2011) to  $Fe^{3+}$  compounds. In particular, a four-fold GS multiplet was used in the curve-fitting (green curves in Figure 2, panel A (a) and (c)), with the first component falling at 710.5 eV. A further component was also needed to account for a broad signal between the two main spin-orbit components, associated to a shake-up satellite (orange curves in Figure 2, panel A (a) and (c)) (Grosvenor et al., 2004). Both spectra of samples 2h and 24 h are well reconstructed by the adopted  $Fe^{3+}$  multiplet, supporting the presence of this oxidation state for iron.

Nevertheless, one difference between the two spectra is apparent regarding the intensity recorded around 715 eV. Here, as pointed out by Grosvenor et al. (2004) an extra-peak (blue curves in Figure 2, panel A (a) and (c)), additional to the GS multiplet, is sometimes needed to describe Fe compounds. This contribution has been reported to be due to  $Fe^{3+}$  ions confined at the surface of a nanostructured material, here denoted as “surface peak”.

In the analyzed samples this peak appears to slightly shift its position and increases in the 24 h sample, suggesting a probable increase in the surface area of the MOF 24 h. The C 1s regions of MIL-100 (Fe) samples are reported in Figure 2, panel A, curves (b) and (d). In both cases the presence of both an aromatic (peaked at 285.0 eV) and a carboxylate carbon component (peaked at 288.8 eV) can be detected (Pérez et al., 2022). These features are fully

compatible with the expected presence of BTC ligands in the MIL-100(Fe) samples. Overall, XPS showed that both MOF samples are constituted by  $Fe^{3+}$  metal centers coordinated by BTC ligands, with the only small, yet significant, difference in the surface component, associated to a probable more nanostructured morphology in the MOF 24 h sample.

Raman spectroscopy was utilized to confirm the synthesis of MIL (100)-Fe at the two synthesis times. Both Raman spectra perfectly matches with the spectrum reported in literature for MIL (100)-Fe, showing the following principal peaks (Li et al., 2016):  $\approx 810$  ( $\nu_{C-H}$ ),  $\approx 1004$  and  $\approx 1610$  ( $\nu_{C=C}$ ),  $\approx 1460$  ( $\nu_{COO^-}$ ) &  $\approx 1550$  ( $\nu_{COO^-}$ ),  $\approx 1370$  ( $\nu_{COOH}$ ), and  $\approx 1216$  (C-O-Fe stretching of trimesate) (Figure 2, panel B). It is interesting to note that the two spectra are very similar to each other, with only a slight difference in the spectral region  $200\text{--}600\text{ cm}^{-1}$  for MOF 2 h, where are visible two peaks, one sharp at  $\approx 250\text{ cm}^{-1}$  and a more widened peak between  $400\text{--}500\text{ cm}^{-1}$ , which are not present in the spectrum of MOF 24 h, probably due to the presence of still unreacted starting materials in the sample.

### 3.2 Electrochemical characterization of modified electrodes

The electrochemical characterization of the modified electrode platforms was performed by CV and EIS in 0.1 M KCl solution containing 5 mM  $Fe(CN)_6^{3-/4-}$ . Figure 3 shows the CVs and Nyquist plots of bare (black), AuNPs (green), MOF2h (blue) and AuNPs/MOF2h (red) GPH/SPE, respectively.

As shown in Figure 3, panel A, all CV curves show two well-defined redox peaks, indicating a fast electron transfer of the redox probe. The peak current increase after the modification of the electrode with AuNPs or MOF is quite small and of similar intensity, whereas a larger increase in the peak current is

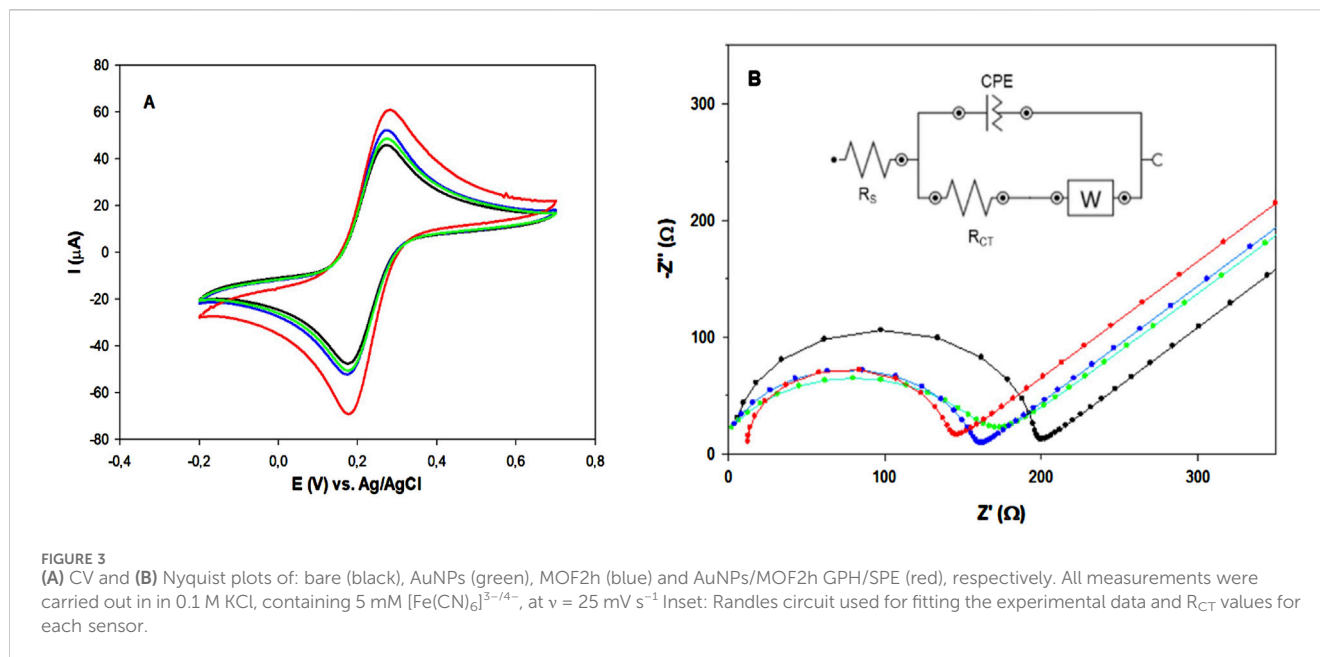


TABLE 1 Electrochemical parameters of unmodified and modified GPH/SPEs: peak-to-peak potential separation ( $\Delta E_p$ ), ratio anodic/cathodic peak current ( $I_{ap}/I_{cp}$ ), electroactive area ( $A_{ea}$ ), roughness factor ( $\rho$ ) and heterogeneous electron transfer rate constant  $k^0$ . Geometric area ( $A_0$ ) =  $0.11 \text{ cm}^2$ .

GPH/SPE	$\Delta E_p$ (mV)	$I_{ap}^*/I_{cp}$ ( $\mu\text{A}$ )	$E_{1/2}$ (mV)	$A_{ea}$ ( $\text{cm}^2$ )	$\rho$	$k^0$ ( $\text{cm s}^{-1}$ )
bare	100	1.14	48	0.132	1.2	$2.11 \pm 0.27 \times 10^{-3}$
AuNPs	99	1.02	58	0.265	2.41	$2.41 \pm 0.40 \times 10^{-3}$
MOF2h	101	1.03	52	0.179	1.63	$2.50 \pm 0.37 \times 10^{-3}$
AuNPs/MOF2h	86	1.06	51	0.327	2.97	$4.30 \pm 0.16 \times 10^{-3}$

\* $v = 25 \text{ mV s}^{-1}$

observed when the two nanomaterials are combined (red curve). A marked decrease in  $\Delta E_p$  was also observed in this case, with the lowest  $\Delta E_p$  value closer to the theoretical value of 59 mV for a one-electron reversible mediator. Table 1 shows all the electrochemical parameters. The electroactive areas of bare and modified GPH/SPEs were calculated by recording CVs in the range 5–500  $\text{mV s}^{-1}$ , according to the Randles-Sevcik Equation 1 (Savan, 2020):

$$I_p = 2.69 \times 10^5 n^{3/2} A_e D^{1/2} C v^{1/2} \quad (1)$$

In equation,  $I_p$  represents the anodic/cathodic peak current (A),  $A_e$  the electroactive area ( $\text{cm}^2$ ),  $D$  the diffusion coefficient ( $7.6 \times 10^{-6} \text{ cm}^2 \text{ s}^{-1}$ ) and  $C$  the concentration ( $2.5 \times 10^{-3} \text{ mol cm}^{-3}$ ) of  $[\text{Fe}(\text{CN})_6]^{3-/4-}$  redox probe in KCl solution,  $n$  is the number of the electrons transferred during the redox reaction ( $n = 1$ ), and  $v$  is the scan rate ( $\text{V s}^{-1}$ ). On the basis of this equation, the  $A_e$  values of MOF2h and AuNPs/MOF2h modified GPH/SPEs resulted to be  $0.179 \text{ cm}^2$  and  $0.327 \text{ cm}^2$  (about 1.3 and 2.5 times higher than bare electrode, respectively (Table 1)). These results indicate that the modification of the bare electrode with MOF2h slightly increases the  $A_e$ , which results marked increased after the adding of AuNPs, attesting that the dispersion of AuNPs on a MOF surface greatly affects the catalytic activity of the material.

The heterogeneous electron transfer rate constant  $k^0$  has also been calculated before and after each modification step, using the Lavagnini et al. method, which merges the Klingler-Kochi and Nicholson and Shain methods for irreversible and reversible systems, respectively (Lavagnini et al., 2004). It is interesting to note that the  $k^0$  value obtained for the AuNPs/MOF2h/GPH/SPE resulted more than 2 times higher than that calculated for the bare one (Table 1). This value confirms the synergistic contributions of MOF and AuNPs, which enhance each other properties: MOF can enhance the porosity and catalytic activity of AuNPs, whereas AuNPs are able to enhance the electrical conductivity of the nanoporous MOF.

The superior electrochemical performances shown by MOF2h both in absence and presence of AuNPs compared to MOF12 h and MOF24 h were demonstrated by CV experiments. The results are reported in Supplementary Figures S2, S3, in absence and in presence of AuNPs, respectively. These results can be ascribed to the most abundant catalytic sites and the large number of defects present in the amorphous/semi-crystalline MOF structure, typical of MOF2h, compared to crystalline MOF12 h and 24 h, which can fasten the electron transfer and lead to a significant enhancement of the catalytic performance (Dissegna et al., 2018; Bechis et al., 2022;

TABLE 2 EIS fitting parameters obtained from the equivalent circuit and  $k^0$  values of unmodified and modified GPH/SPEs.

GPH/SPE	$R_s$ ( $\Omega$ )	$R_{CT}$ ( $\Omega$ )	CPE (nMho s <sup>N</sup> )	N	W (mMho s <sup>1/2</sup> )	$k^0$ (cm s <sup>-1</sup> )
bare	4.69	194	5.43	1.01	1.67	$4.99 \times 10^{-3}$
AuNPs	3.44	178	6.56	1.03	1.76	$5.44 \times 10^{-3}$
MOF2h	1.86	168	7.57	1	1.31	$5.76 \times 10^{-3}$
AuNPs/MOF2h	8.74	145	18	0.94	2.18	$5.90 \times 10^{-3}$

Dong et al., 2022; Zhao et al., 2024). On the basis on the results obtained, the MOF2h was used for further experiments, and referred as MOF.

The kinetic mechanism of the electrochemical reaction at AuNPs/MOF/GPH/SPE modified electrode was also investigated by monitoring the relationship between scan rate and peak current (Supplementary Figure S4A). It can be observed a shift of the anodic and cathodic peaks towards more positive and negative potentials, respectively, when the scan rate is increased from 5 to 200 mV s<sup>-1</sup>, due to the effect of the resistance of the electrode. A linear relationship was also found between the peak magnitude of the anodic and cathodic current of the modified sensor and the square root of the scan rate (Supplementary Figure S4B), indicating that the electrochemical process is diffusion-controlled.

EIS measurements were also performed for a further electrochemical characterization of the proposed platforms. The EIS spectra were recorded in the frequency range 1–500 kHz. The semicircle diameter in the high frequency region corresponds to the charge transfer resistance (RCT). The corresponding Nyquist plots are shown in Figure 3, panel B. The bare electrode (black curve) exhibited the highest RCT value. The AuNPs modified electrode (green curve) showed a slightly lower RCT value, suggesting improved conductivity. Similar behavior was obtained with MOF modified electrode (blue curve). It can be observed that the RCT value of the MOF electrode is a little larger than that of the AuNPs electrode. These results confirm the better conductivity of both nanomaterials, with small superior performances exhibited by the semi-amorphous MOF2h. Finally, a more significant decrease in RCT value is observed with the AuNPs/MOF/GPH/SPE (red curve), attesting the increased electrical conductivity when both nanomaterials are combined in a hybrid nanocomposite, in perfect agreement with the results obtained with CV.

All data obtained were fitted by applying the Randles circuit (Figure 3, panel B, inset) and the results are reported in Table 2. Based on the RCT values obtained for bare and modified GPH/SPEs, the  $k^0$  of the redox probe between the bulk solution and the sensor surface for each electrode was calculated by Equation 2:

$$K^0 = \frac{RT}{R_{CT}F^2n^2AC} \quad (2)$$

where R is the universal gas constant (8.314 J K<sup>-1</sup> mol<sup>-1</sup>), T the temperature (298.15 K), F F's constant (96,485 C mol<sup>-1</sup>), n the number of transferred electrons, A the electrode geometric area (0.11 cm<sup>2</sup>), and C the redox probe concentration ( $2.5 \times 10^{-6}$  mol cm<sup>-3</sup>).

The calculated  $k^0$  values agree with the RCT ones (Table 2), attesting a strong synergistic effect of the two nanomaterials that

create a hybrid nanocomposite with superior electrochemical performances. As for the other Randles parameters, the constant phase element (CPE) is a parameter usually related to surface reactivity, electrode porosity, roughness, and surface inhomogeneity, and therefore it was expected that this value would rise from 5.43 for bare electrode to 18 n MhO s<sup>N</sup> for AuNPs/MOF/GPH/SPE electrode, due to its greater structural complexity (Jorcin et al., 2006).

### 3.3 Voltammetric response of testosterone at AuNPs/MOF/GPH/SPE electrode

Figure 4 shows an irreversible cathodic peak for testosterone reduction at a potential of about -0.4 V vs. Ag/AgCl at a fixed testosterone concentration (0.1  $\mu$ M).

The scan rate effect on the cathodic peak current response of the AuNPs/MOF/GPH/SPE sensor has been investigated at the same fixed testosterone concentration in the range 2–25 mV s<sup>-1</sup> and a linear relationship between the peak current values and the scan rate has been obtained, attesting a typical adsorption process at the solution/sensor interface for TST reduction (Figure 4 inset) (Tortolini et al., 2022; Kozak et al., 2022). The logarithm of the peak current of testosterone vs. log  $\nu$  is also reported in Supplementary Figure S5. The slope value resulted to be 0.945, typical value of a total absorption process (value close to 1.0) (Tortolini et al., 2024b).

The surface coverage ( $\Gamma$ ) of testosterone onto the AuNPs/MOF/GPH/SPE was calculated from the plot of  $I_p$  versus scan rate  $\nu$ , according to Equation 3 (Laviron, 1979):

$$I_p = n^2F^2Av\Gamma/4RT \quad (3)$$

where n is the number of electrons, F, R, and T are the Faraday constant, the molar gas constant, and the absolute temperature,  $\nu$  is the scan rate, and  $\Gamma$  the surface coverage. Assuming n = 2 for testosterone (Levent et al., 2015), its  $\Gamma$  value was found to be  $0.011 \times 10^{-8}$  mol cm<sup>-2</sup>, with a similar order of magnitude of  $\Gamma$  values calculated for TST with different electrodes reported in literature (Kozak et al., 2022).

#### 3.3.1 Effect of pH

The influence of the pH on the electrochemical response of testosterone on the electrode surface was performed in the pH range 2–9, using acetate, Britton-Robinson, PBS and borate buffer (all 0.1 M) in presence of 0.1  $\mu$ M testosterone. The cathodic peak currents and the potential of peak currents are plotted versus pH (Figure 5). An increase in cathodic peak current ( $I_{pc}$ ) value

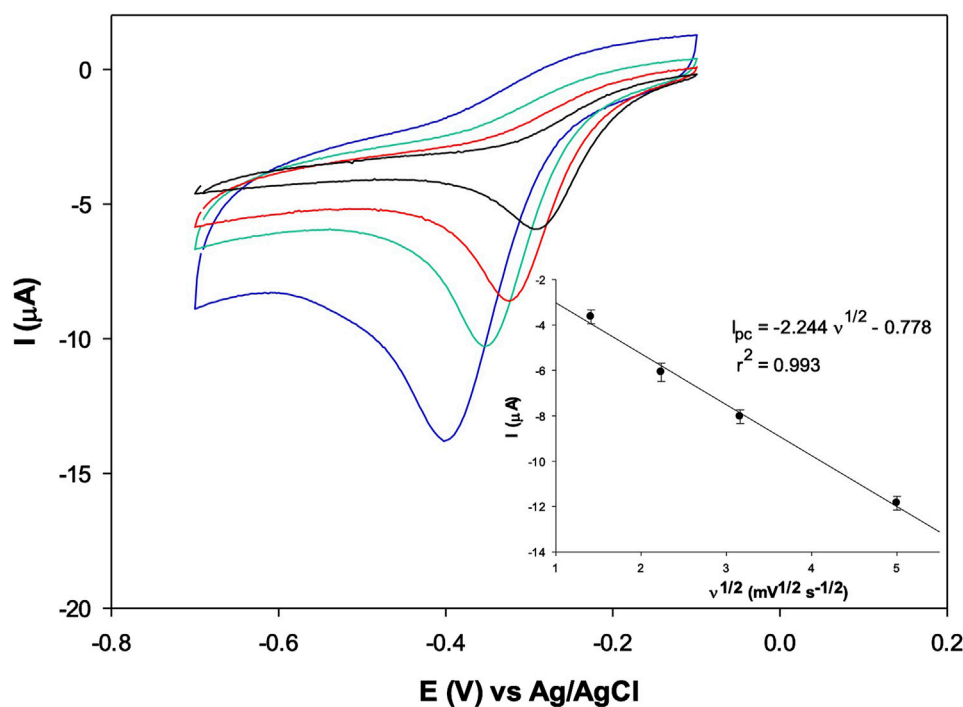


**FIGURE 4**  
CVs of 0.1  $\mu\text{M}$  testosterone, with AuNPs/MOF2h/GPH/SPE at the scan rate: 2 (black), 5 (red), 10 (green) and 25 (blue)  $\text{mV s}^{-1}$  in PBS. In the inset, the plot of the cathodic peak current vs. scan rate ( $n = 3$ ).

was observed between pH 2 and 7, with a decrease at higher values (red curve). Basing on the obtained data, the best current signal was obtained at pH 7 in PBS, and therefore this pH value was selected as optimum pH value and used for further investigation. These results are in good agreement with data reported in literature (Huang and Feng, 2024) and are of particular interest for possible biosensing applications as they mimic the physiological conditions. The potential showed also a linear dependence on pH, with a progressive cathodic peak potential ( $E_{\text{pc}}$ ) shift towards negative values by decreasing pH, as shown in Figure 5 (blue curve). The plot of  $E_{\text{pc}}$  vs. pH gave a straight line with the following corresponding equation:  $E_{\text{pc}} (\text{V}) = -0.029 \text{ pH} - 0.215$ ,  $R^2 = 0.993$ . The slope value of the linear fit (0.029 V) confirms a mechanism with 2 electrons involved in the electrocatalytic reduction of testosterone on the modified sensor, in agreement with the overall reaction pathway, shown in Figure 6, involving two electrons and two protons, already reported in literature (Levent et al., 2015), which suggested a 3 step process: 1) one-electron reduction of the C-3 keto group to produce unprotonated radical; 2) protonation; 3) reaction with another molecule to produce a dimeric structure.

### 3.4 Determination of energy levels and sensing mechanism

For a further in-depth analysis about the sensing of testosterone, the energy levels (HOMO–LUMO) of testosterone and AuNPs/MOF were evaluated, respectively, using CV technique, by applying

potentials above the LUMO or below the HOMO (vs. Ag/AgCl), leading to cathodic and anodic currents, respectively, that can be used for the determination of LUMO and HOMO.

The CV measurements were carried out first for a bare glassy carbon electrode (GCE) before and after the drop-casting of 10  $\mu\text{L}$  of MOF and 10  $\mu\text{L}$  of AuNPs and represented in Figure 7, panel A. The oxidation and reduction peak potentials were used for determination of the EHOMO and ELUMO using the Equations 4–6.

$$E_{\text{HOMO}} = -e (E_{\text{Ox vs NHE}} + 4.75) (\text{eV}) \quad (4)$$

$$E_{\text{LUMO}} = -e (E_{\text{Red vs NHE}} + 4.75) (\text{eV}) \quad (5)$$

$$E_{\text{NHE}} = E_{\text{Ag/AgCl}} + 0.197 (\text{eV}) \quad (6)$$

The working electrode indicates a reduction peak at  $-1.2 \text{ V}$  and an oxidation peak at  $0.6 \text{ V}$  vs. Ag/AgCl.

The ELUMO and EHOMO resulted to be  $-3.75 \text{ eV}$  and  $-5.55 \text{ eV}$ , respectively. The band gap energy between ELUMO and EHOMO was calculated to be  $1.8 \text{ eV}$ . The ELUMO and EHOMO values for testosterone are reported in literature (Kumari et al., 2021). As shown in Figure 7, panel B, after applying a positive voltage to the system, the electrode potential energy dropped. Then, the electrons were transferred from AuNPs/MOF to the GCE surface (step 1). The HOMO levels of AuNPs/MOF and testosterone are well-matched to efficiently promote the electron transfer from testosterone to the electron-deficient AuNPs/MOF (step 2), thus leading to the testosterone reduction. These results confirm that the AuNPs/MOF may represent a favorable nanomaterial to provide fast electron transfer processes.

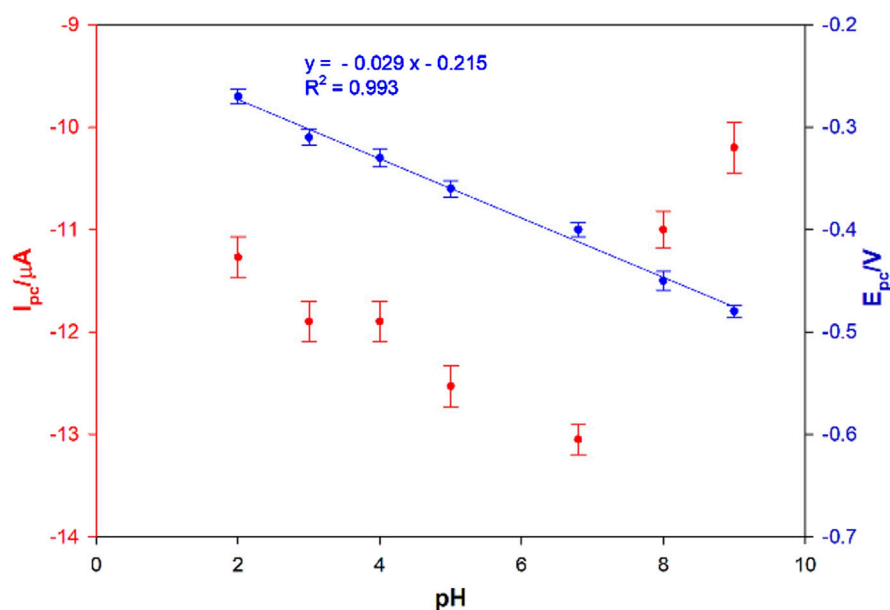


FIGURE 5 Influence of pH and potential on the cathodic peak current for 0.1  $\mu M$  testosterone at the AuNPs/MOF/GPH/SPE sensor ( $n = 25 \text{ mV s}^{-1}$ ,  $n = 3$ ).

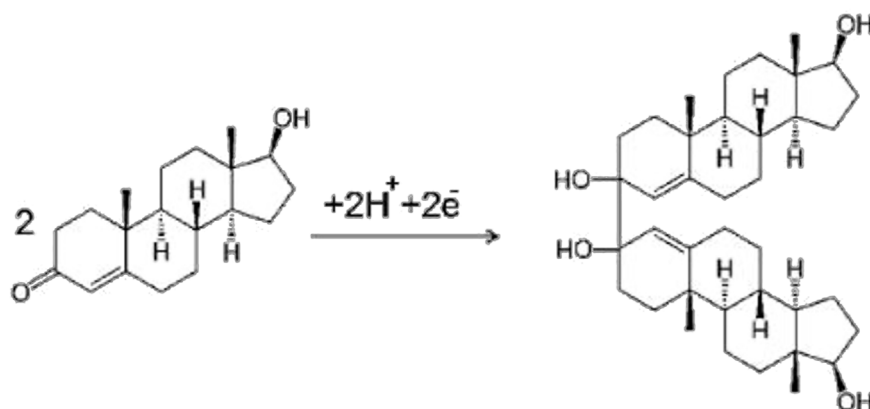


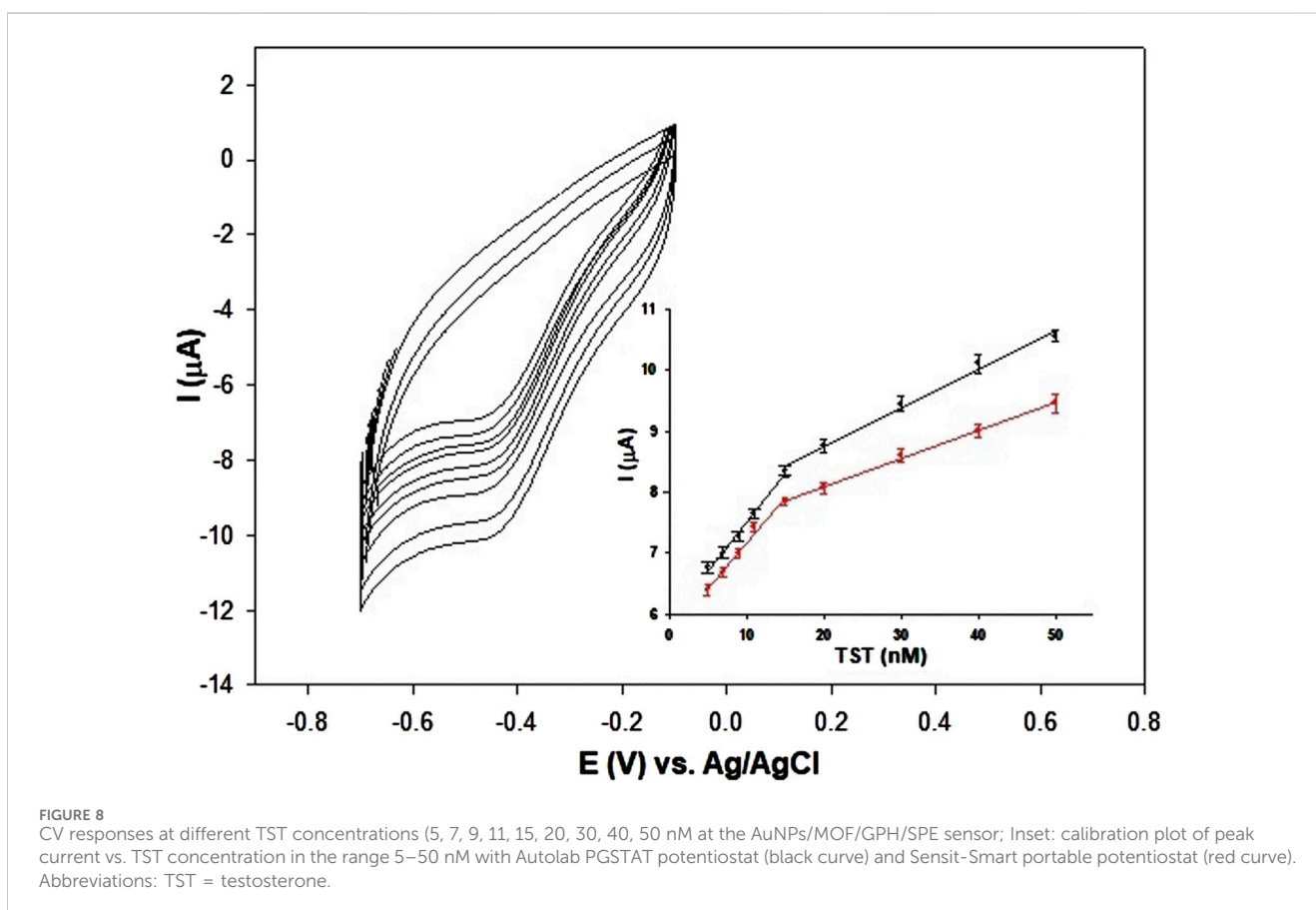
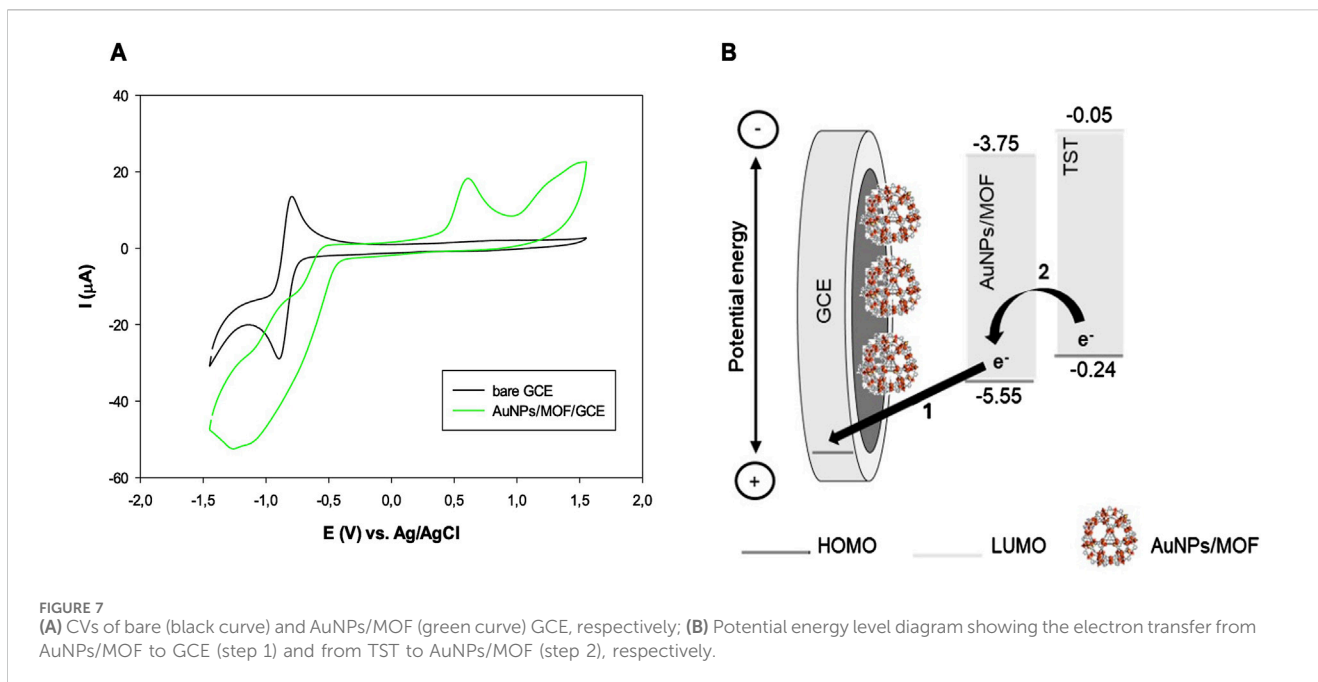
FIGURE 6 Mechanism of the reduction process of testosterone.

On the basis of the HOMO level of MIL-100(Fe) reported in literature ( $-1.38 \text{ eV}$ ) (Rojas-Guerrero et al., 2023), it is interesting to note that that energy gap between testosterone and AuNPs/MO nanomaterial is much higher compared to MOF without the modification with AuNPs, thus attesting a favoured electron transfer.

### 3.5 Testosterone detection at AuNPs/MOF/GPH/SPE

The analytical performances of the AuNPs/MOF/GPH/SPE towards different testosterone concentration (from 5 to 50 nM)

were investigated by CV technique (Figure 8), and the peak values were used for the construction of the sensor calibration curve (Figure 8, inset). The proposed electrochemical sensor shows a linear response over the range of 5–50 nM with the following two linear regression equations (black curves):  $\Delta I_p$  ( $\mu A$ ) = 0.160 CTST (nM) + 5.90 ( $R^2 = 0.992$ ) and  $\Delta I_p$  ( $\mu A$ ) = 0.063 CTST (nM) + 7.48 ( $R^2 = 0.991$ ) and a detection limit (LOD) of 2 nM, calculated on Formula 3  $\sigma/S$ , where  $\sigma$  represents the blank standard deviation and  $S$  the calibration slope. All measurements were made in triplicate and the results reported as mean values. Figure 8 inset shows also the calibration plot (red curves) obtained with a portable potentiostat, directly connected to a smartphone for POC signal reading, named



Sensit-Smart. Once again, two linear regression equations are obtained:  $\Delta I_p (\mu A) = 0.149 \text{ CTST (nM)} + 5.67$  ( $R^2 = 0.990$ ) and  $\Delta I_p (\mu A) = 0.046 \text{ CTST (nM)} + 7.16$  ( $R^2 = 0.998$ ) and a slightly

higher LOD of 3 nM. Differential pulse voltammetry (DPV) has also used to test the results obtained with CV. The DPV curves and the relative calibration plots are reported in [Supplementary](#)

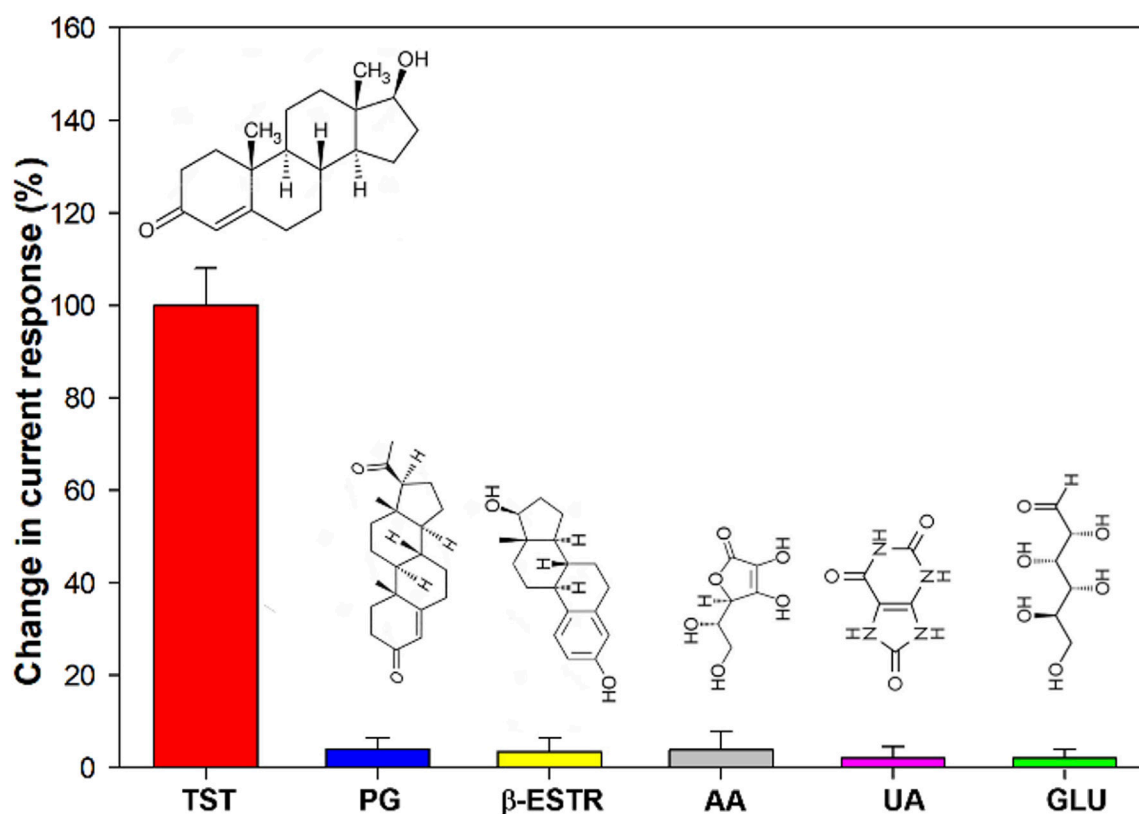


FIGURE 9 Histogram of the selectivity of AuNPs/MOF/GPH/SPE sensor for TST detection. TST = testosterone; PG = progesterone;  $\beta$ -ESTR =  $\beta$ -estradiol; AA = ascorbic acid; UA = uric acid; GLU = glucose.

Figures S6A, B. The sensor shows a slightly larger linear range between 1–50 nM with the following two linear regression equations (dotted curves):  $\Delta I_p$  ( $\mu\text{A}$ ) = 0.74 CTST (nM) + 3.17 ( $R^2 = 0.992$ ) and  $\Delta I_p$  ( $\mu\text{A}$ ) = 0.44 CTST (nM) + 13.90 ( $R^2 = 0.991$ ), and a detection limit (LOD) of 0.5 nM, calculated with the same Formula 3  $\sigma/S$ , reported above. The sensibility and LODs were definitely improved, as expected by employing a more sensitive technique.

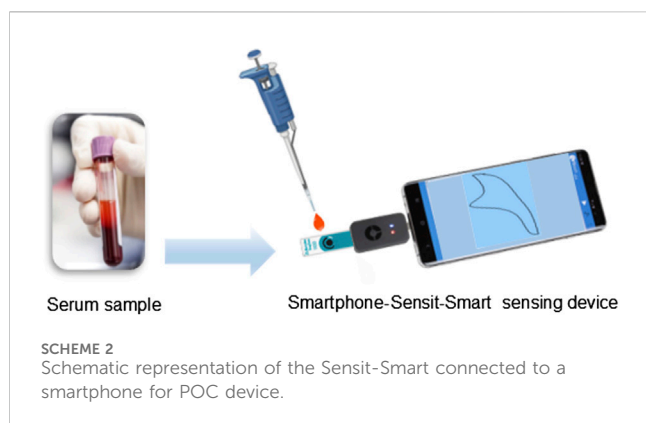
In addition, a comparison with other electrochemical (bio) sensors reported in literature for testosterone detection has been reported, and the results are summarized in Supplementary Table S1. Most of them are electrochemical sensors (Goyal et al., 2010; Levent et al., 2014; Moura et al., 2014; Gugoasa et al., 2015; Liu et al., 2017; Kellens et al., 2018; Lee et al., 2019; Sanli et al., 2020) and only three of them (last three rows in Supplementary Table S1) are immunosensors (Eguilaz et al., 2010; Serafin et al., 2011; Bulut et al., 2020). The developed sensor shows analytical performances not better than but comparable to most other recently developed sensors and immunosensors. In particular, among the electrochemical sensor, a recent study (Huang and Feng, 2024) describes another MOF-based sensor with  $\text{Cu}^{2+}$  instead of  $\text{Fe}^{3+}$  as metal ion. The Cu-MOF was coupled with rGO to form a hybrid rGO/Cu-MOF nanomaterial, which shows slightly superior performances compared to the MIL-100(Fe)-based sensor used in this study, but it must be remarked that

MIL-100(Fe) has been synthesized according to a total ecofriendly synthetic method (room temperature compared to 150°C of Cu-MOF synthesis), with a much shorter synthesis time (2 h compared to 36 h) and without the use of any organic solvent, unlike Cu-MOF synthesis in which dimethyl formamide was employed.

### 3.6 Reproducibility and stability of AuNPs/MOF/GPH/SPE sensor

The reproducibility of the final platform has been tested by using five electrodes ( $n = 3$ ) and recording the current signal obtained with each of them by CV technique in presence of 50  $\mu\text{M}$  testosterone solution. The relative standard deviation (RSD) value obtained is 1.2%, suggesting a good fabrication reproducibility of the AuNPs/MOF GPH/SPE platform (Supplementary Figure S7).

Finally, the stability of the developed sensor has also been investigated. Five different electrodes, stored at 4°C, were tested every 5 days for 1 month, by measuring the CV signal obtained for a 0.1  $\mu\text{M}$  testosterone solution ( $n = 3$ ). The results show that sensors used on day 5, 10, 15, 20, 25, and 30 show a current signal decrease lower than 15%, compared to the response of the electrodes used on day 0 (Supplementary Figure S8).



### 3.7 Selectivity

The selectivity was assessed by investigating the effect of possible interfering compounds commonly found in biological fluids, such as glucose, uric acid, ascorbic acid,  $\beta$ -estradiol and progesterone.

Figure 9 shows the current response towards these other compounds at a 10-times higher concentration and no significant signal change was registered (signal change less than 4.0%), confirming the excellent selectivity of the proposed sensor.

### 3.8 Testosterone detection in real human serum samples

The matrix effect of five real samples of human serum was tested with the proposed sensor by using a standard addition method and the smartphone-Sensit/Smart potentiostat based sensing device. The schematic representation of the smartphone based sensing device is represented in Scheme 2.

All measurements were performed with 150  $\mu$ L of serum samples, prepared as described in the experimental part, and placed directly on the modified SPE surface. The measurements were performed in triplicate by CV technique. The results showed a good recovery with recovery rates in the range 98.5%–103.7% for all spiked real samples, with RSD values lower than 4% after three replicate measurements for each sample (Table 3).

These results demonstrate the absence of matrix effect and therefore the potential for the proposed platform for numerous

biomedical applications, both in clinical diagnosis and doping control analysis.

## 4 Conclusion

In summary, the suitability of a novel ecofriendly electrochemical platform based on AuNPs and MIL-100(Fe) drop-casted onto a graphene SPE for the development of a testosterone sensor has been demonstrated. MIL-100(Fe) showed several advantages when used as an electrode modifier: 1) Fe is a biocompatible and a safe metal for human applications; 2) it can be synthesized by a “short time” green method. In particular, we have demonstrated that the MOF with a synthesis time of 2 h, showed a semi-amorphous nature and enhanced electroconductive properties compared to MOF 24 h, with a higher degree of crystallinity, in absence and in presence of AuNPs. These results can be ascribed to the superior electron transfer capabilities of semi-amorphous MOFs, probably thanks to a plethora of defects and more accessible active sites.

As a proof of concepts, this work demonstrates the use of a AuNPs/MOF2h/GPH/SPE sensor for the detection of testosterone in the range 1–50 nM, which is within the physiological range of serum testosterone for a healthy male. These results are due to the synergistic effect of high conductive AuNPs and highly porous MOF. The resulting hybrid nanomaterial, AuNPs/MOF, shows improved electrochemical properties thanks to the advantages of both materials: possibility for better analyte adsorption thanks to the highly porous nature of MOF, and high electrical conductivity, which allows fast and effective electron transfer, thanks to AuNPs.

The proposed nanocomposite-based sensor showed also a good selectivity towards some structurally similar compounds and other endogenous compounds and a long-term stability.

Finally, the applicability of the proposed sensor interfaced with a miniaturized potentiostat (Sensit-Smart) for POC detection was tested in spiked samples of human serum of five healthy male volunteers showing good recovery values, and very good results, with great potential for application in clinical diagnostics and in doping control.

Moreover, to the best of our knowledge, this is the first sensor for testosterone detection based on a semi-amorphous MOF. Therefore, the excellent results obtained position semi-amorphous MOFs as novel valuable assets for developing advanced (bio)sensors for the

TABLE 3 Results of CV analyses using AuNPs/MOF/GPH/SPE of real human serum samples diluted in 0.1 M PBS, utilizing the Sensit/Smart potentiostat.

Sample	TST spiked (nM)	TST detected (nM)	Recovery (%) <sup>*</sup>	RSD (%; n = 3)
Serum 1	10.0	10.3	103.0	2.2
Serum 2	15.0	14.8	98.7	3.2
Serum 3	20.0	19.7	98.5	2.5
Serum 4	25.0	24.8	99.2	3.8
Serum 5	30.0	31.1	103.7	2.9

<sup>\*</sup>Recovery (%) = ([Found]/[Added])  $\times$  100.

detection of other endogenous substances, thus broadening the scope of their catalytic applications.

## Data availability statement

The raw data supporting the conclusions of this article will be made available by the authors, without undue reservation.

## Ethics statement

Ethical approval was not required for the studies, the serum samples were provided by five healthy volunteers. The studies were conducted in accordance with the local legislation and institutional requirements. The participants provided their written informed consent to participate in this study.

## Author contributions

CT: Data curation, Investigation, Methodology, Writing–original draft. FB: Writing–original draft, Funding acquisition. DP: Investigation, Writing–original draft. AM: Investigation, Writing–original draft. AI: Funding acquisition, Writing–review and editing. DG: Funding acquisition, Writing–review and editing. RA: Conceptualization, Supervision, Writing–review and editing.

## Funding

The author(s) declare that financial support was received for the research, authorship, and/or publication of this article. This work was supported by the Italian grant PRIN 2020 (Prot. 20203AMKTW\_003 – CUP J75E22000310008).

## References

- Alam, M. M., Rahman, M. M., Asiri, A. M., and Fazal, M. A. (2021). A reliable electrochemical approach for detection of testosterone with CuO-doped CeO<sub>2</sub> nanocomposites-coated glassy carbon electrode. *J. Mater. Sci. Mater. Electron.* 32, 5259–5273. doi:10.1007/s10854-021-05257-2
- Alvarado, L. C. (2010). Population differences in the testosterone levels of young men are associated with prostate cancer disparities in older men. *Am. J. Hum. Biol. official J. Hum. Biol. Council.* 22 (4), 449–455. doi:10.1002/ajhb.21016
- Ayati, A., Shahrak, M. N., Tanhaei, B., and Sillanpää, M. (2016). Emerging adsorptive removal of azo dye by metal-organic frameworks. *Chemosphere* 160, 30–44. doi:10.1016/j.chemosphere.2016.06.065
- Bahrani, E., Amini, R., and Vardak, S. (2021). Electrochemical detection of dopamine via pencil graphite electrodes modified by Cu/Cu<sub>2</sub>O nanoparticles. *J. Alloys Compd.* 855 (2), 157292. doi:10.1016/j.jallcom.2020.157292
- Barroso, O., Mazzoni, I., and Rabin, O. (2008). Hormone abuse in sports: the antidoping perspective. *Asian J. Androl.* 10 (3), 391–402. doi:10.1111/j.1745-7262.2008.00402.x
- Bechis, I., Sapnik, A. F., Tarzia, A., Wolpert, E. H., Addicoat, M. A., Keen, D. A., et al. (2022). Modeling the effect of defects and disorder in amorphous metal-organic frameworks. *Chem. Mater.* 34 (20), 9042–9054. doi:10.1021/acs.chemmater.2c01528
- Berglund, L. H., Prytz, H. S., Perski, A., and Svartberg, J. (2011). Testosterone levels and psychological health status in men from a general population: the Tromsø study. *aging male official J. Int. Soc. Study Aging Male* 14 (1), 37–41. doi:10.3109/13685538.2010.522276
- Bhasin, S., Woodhouse, L., and Storer, T. W. (2001). Proof of the effect of testosterone on skeletal muscle. *J. Endocrinol.* 170 (1), 27–38. doi:10.1677/joe.0.1700027
- Biesinger, M. C., Payne, B. P., Grosvenor, A. P., Lau, L. W. M., Gerson, A. R., and Smart, R. S. C. (2011). Resolving surface chemical states in XPS analysis of first row transition metals, oxides and hydroxides: Cr, Mn, Fe, Co and Ni. *Appl. Surf. Sci.* 257, 2717–2730. doi:10.1016/j.apsusc.2010.10.051
- Bozdoğan, B. (2023). Electrochemical testosterone biosensor based on pencil graphite electrode electrodeposited with copper oxide nanoparticles. *Meas. Sci. Technol.* 34, 105106. doi:10.1088/1361-6501/ace126
- Bulut, U., Sanli, S., Cevher, S. C., Cirpan, A., Donmez, S., and Timur, S. (2020). A biosensor platform based on amine functionalized conjugated benzenediamine-benzodithiophene polymer for testosterone analysis. *J. Appl. Polym. Sci.* 137, e49332. doi:10.1002/app.49332
- Delpiano, G. R., Tocco, D., Medda, L., Magner, E., and Salis, A. (2021). Adsorption of malachite green and alizarin red S dyes using Fe-BTC metal organic framework as adsorbent. *Int. J. Mol. Sci.* 22 (2), 788. doi:10.3390/ijms22020788
- Dissegna, S., Epp, K., Heinz, W. R., Kieslich, G., and Fischer, R. A. (2018). Defective metal-organic frameworks. *Adv. Mater.* 30 (37), 1704501. doi:10.1002/adma.201704501
- Dolgoplova, E. A., Rice, A. M., Martin, C. R., and Shustova, N. B. (2018). Photochemistry and photophysics of MOFs: steps towards MOF-based sensing enhancements. *Chem. Rev.* 47 (13), 4710–4728. doi:10.1039/C7CS00861A
- Dong, J., Lv, C., Humphrey, M. G., Zhang, C., and Huang, Z. (2022). One-dimensional amorphous cobalt(ii) metal-organic framework nanowire for efficient

## Acknowledgments

We acknowledge Francesco Amato for his support in performing Raman measurements.

## Conflict of interest

The authors declare that the research was conducted in the absence of any commercial or financial relationships that could be construed as a potential conflict of interest.

The author(s) declared that they were an editorial board member of Frontiers, at the time of submission. This had no impact on the peer review process and the final decision.

## Generative AI statement

The author(s) declare that no Gen AI was used in the creation of this manuscript.

## Publisher's note

All claims expressed in this article are solely those of the authors and do not necessarily represent those of their affiliated organizations, or those of the publisher, the editors and the reviewers. Any product that may be evaluated in this article, or claim that may be made by its manufacturer, is not guaranteed or endorsed by the publisher.

## Supplementary material

The Supplementary Material for this article can be found online at: <https://www.frontiersin.org/articles/10.3389/fsens.2025.1527587/full#supplementary-material>

- hydrogen evolution reaction. *Inorg. Chem. Front.* 9 (16), 4184–4193. doi:10.1039/D2Q100473A
- Eguilaz, M., Moreno-Guzmán, M., Campuzano, S., González-Cortés, A., Yáñez-Sedeño, P., and Pingarrón, J. M. (2010). An electrochemical immunosensor for testosterone using functionalized magnetic beads and screen-printed carbon electrodes. *Biosens. Bioelectron.* 26, 517–522. doi:10.1016/j.bios.2010.07.060
- Fourou, H., Braiek, M., Bonhomme, A., Lagarde, F., Zazoua, A., and Jaffrezic-Renault, N. (2018). Voltammetric sensor based on a double-layered molecularly imprinted polymer for testosterone. *Anal. Lett.* 51, 312–322. doi:10.1080/00032719.2017.1298118
- Ghanbari, T., Abnisa, F., and Wan Daud, W. M. A. (2020). A review on production of metal organic frameworks (MOF) for CO<sub>2</sub> adsorption. *Sci. total Environ.* 707, 135090. doi:10.1016/j.scitotenv.2019.135090
- Goyal, R. N., Gupta, V. K., and Chatterjee, S. (2010). Electrochemical investigations of corticosteroid isomers-testosterone and epitestosterone and their simultaneous determination in human urine. *Anal. Chim. Acta.* 657, 147–153. doi:10.1016/j.aca.2009.10.035
- Grosvenor, A. P., Kobe, B. A., Biesinger, M. C., and McIntyre, N. S. (2004). Investigation of multiplet splitting of Fe 2p XPS spectra and bonding in iron compounds. *Surf. Interface Analysis* 36, 1564–1574. doi:10.1002/sia.1984
- Guesh, K., Caiuby, C. A. D., Mayoral, A., Diaz-Garcia, M., Diaz, I., and Sánchez-Sanchez, M. (2017). Sustainable preparation of MIL-100(Fe) and its photocatalytic behavior in the degradation of methyl orange in water. *Cryst. Growth and Des.* 17, 1806–1813. doi:10.1021/acs.cgd.6b01776
- Guoasa, L. A., Stefan-van Staden, R. I., Calenic, B., and Legler, J. (2015). Multimode sensors as new tools for molecular recognition of testosterone, dihydrotestosterone and estradiol in children's saliva. *J. Mol. Recognit.* 28 (1), 10–19. doi:10.1002/jmr.2408
- Gupta, R. P., and Sen, S. K. (1974). Calculation of multiplet structure of core p-vacancy levels. *Phys. Rev. B* 10 (1), 71–77. doi:10.1103/PhysRevB.10.71
- Gupta, R. P., and Sen, S. K. (1975). Calculation of multiplet structure of core p-vacancy levels. *II Phys. Rev. B* 12 (1), 15–19. doi:10.1103/PhysRevB.12.15
- Han, L., Qi, H., Zhang, D., Ye, G., Zhou, W., Hou, C., et al. (2017). A facile and green synthesis of MIL-100(Fe) with high-yield and its catalytic performance. *New J. Chem.* 41, 13504–13509. doi:10.1039/C7NJ02975F
- Heidarimoghdam, R., Akhavan, O., Ghaderi, E., Hashemi, E., Mortazavi, S. S., and Farnany, A. (2016). Graphene oxide for rapid determination of testosterone in the presence of cetyltrimethylammonium bromide in urine and blood plasma of athletes. *Mater. Sci. Eng. C* 61, 246–250. doi:10.1016/j.msec.2015.12.005
- Hu, S., Chen, Z., and Zhang, T. (1993). Adsorptive stripping voltammetry of testosterone propionate in pharmaceutical preparations. *Fresenius J. Anal. Chem.* 346, 1008–1010. doi:10.1007/BF00322768
- Huang, S., and Feng, R. (2024). A new electrochemical biosensor based on graphene oxide for rapid detection of synthetic testosterone as performance-enhancing drugs in athletes. *Alex. Eng. J.* 98, 281–289. doi:10.1016/j.aej.2024.04.054
- Jiang, D., Chen, M., Wang, H., Zeng, G., Huang, D., Cheng, M., et al. (2019). The application of different typological and structural MOFs-based materials for the dyes adsorption. *Coord. Chem. Rev.* 380, 471–483. doi:10.1016/j.ccr.2018.11.002
- Jiao, L., Wang, Y., Jiang, H. L., and Xu, Q. (2018). Metal-organic frameworks as platforms for catalytic applications. *Adv. Mater.* 30 (37), e1703663. doi:10.1002/adma.201703663
- Jorcin, J. B., Orazem, M. E., Pébère, N., and Tribollet, B. (2006). CPE analysis by local electrochemical impedance spectroscopy. *Electrochimica Acta* 51, 1473–1479. doi:10.1016/j.electacta.2005.02.128
- Kellens, E., Bové, H., Vandenryt, T., Lambrichts, J., Dekens, J., Drijkoningen, S., et al. (2018). Micro-patterned molecularly imprinted polymer structures on functionalized diamond-coated substrates for testosterone detection. *Biosens. Bioelectron.* 118, 58–65. doi:10.1016/j.bios.2018.07.032
- Kozak, J., Tyszczyk-Rotko, K., Wójciak, M., Sowa, I., and Rotko, M. (2022). Electrochemically pretreated sensor based on screen-printed carbon modified with Pb nanoparticles for determination of testosterone. *Materials* 15 (14), 4948. doi:10.3390/ma15144948
- Kumar, P., Kumar, N., Thakur, D. S., and Patidar, A. (2010). Male hypogonadism: symptoms and treatment. *J. Adv. Pharm. Technol. and Res.* 1 (3), 297–301. doi:10.4103/0110-5558.72420
- Kumari, K., Kumar, A., Bahadur, I., and Singh, P. (2021). Investigate the interaction of testosterone/progesterone with ionic liquids on varying the anion to combat COVID-19: density functional theory calculations and molecular docking approach. *JPOC* 34, e4273. doi:10.1002/poc.4273
- Laczka, O., del Campo, F. J., Muñoz-Pascual, F. X., and Baldrich, E. (2011). Electrochemical detection of testosterone by use of three-dimensional disc-ring microelectrode sensing platforms: application to doping monitoring. *Anal. Chem.* 83 (11), 4037–4044. doi:10.1021/ac1031594
- Lavagnini, I., Antiochia, R., and Magno, F. (2004). An extended method for the practical evaluation of the standard rate constant from cyclic voltammetric data. *Electroanalysis* 16 (6), 505–506. doi:10.1002/elan.200302851
- Laviron, E. J. (1979). General expression of the linear potential sweep voltammogram in the case of diffusionless electrochemical systems. *Electroanal. Chem.* 101, 19–28. doi:10.1016/S0022-0728(79)80075-3
- Lee, M.-H., Thomas, J. L., Liu, W.-C., Zhang, Z.-X., Liu, B. D., Yang, C.-H., et al. (2019). A multichannel system integrating molecularly imprinted conductive polymers for ultrasensitive voltammetric determination of four steroid hormones in urine. *Microchim. Acta.* 186, 695–705. doi:10.1007/s00604-019-3797-7
- Levent, A., Altun, A., Taş, S., Yardım, Y., and Şentürk, Z. (2015). Voltammetric behavior of testosterone on bismuth film electrode: highly sensitive determination in pharmaceuticals and human urine by square-wave adsorptive stripping voltammetry. *Electroanalysis* 27 (5), 1219–1228. doi:10.1002/elan.201400627
- Levent, A., Altun, A., Yardım, Y., and Şentürk, Z. (2014). Sensitive voltammetric determination of testosterone in pharmaceuticals and human urine using a glassy carbon electrode in the presence of cationic surfactant. *Electrochimica Acta* 128, 54–60. doi:10.1016/j.electacta.2013.10.024
- Li, G., Zhu, M., Ma, L., Yan, J., Lu, X., Shen, Y., et al. (2016). Generation of small single domain nanobody binders for sensitive detection of testosterone by electrochemical impedance spectroscopy. *ACS Appl. Mater. Interfaces.* 8, 13830–13839. doi:10.1021/acsami.6b04658
- Li, X., Lachmanski, L., Safi, S., Sene, S., Serre, C., Grenèche, J. M., et al. (2017). New insights into the degradation mechanism of metal-organic frameworks drug carriers. *Sci. Rep.* 7 (1), 13142. doi:10.1038/s41598-017-13323-1
- Liu, B., Peng, Y., Jin, Z., Wu, X., Gu, H., Wei, D., et al. (2023). Terahertz ultrasensitive biosensor based on wide-area and intense light-matter interaction supported by QBIC. *Chem. Eng. J.* 462, 142347. doi:10.1016/j.cej.2023.142347
- Liu, W., Ma, Y., Sun, G., Wang, S., Deng, J., and Wei, H. (2017). Molecularly imprinted polymers on graphene oxide surface for EIS sensing of testosterone. *Biosens. Bioelectron.* 92, 305–312. doi:10.1016/j.bios.2016.11.007
- Lu, G., Duan, L., Meng, S., Cai, P., Ding, S., and Wang, X. (2023). Development of a colorimetric and turn-on fluorescent probe with large Stokes shift for H2S detection and its multiple applications in environmental, food analysis and biological imaging. *Dyes Pigments.* 220, 111687. doi:10.1016/j.dyepig.2023.111687
- Luetjens, C. L., and Weinbauer, F. G. (2012). *Testosterone: biosynthesis, transport, metabolism and (non-genomic) actions.* Cambridge: Cambridge University Press. doi:10.1017/CBO9781139003353.003
- Ma, Y., Leng, Y., Huo, D., Zhao, D., Zheng, J., Yang, H., et al. (2023). A sensitive enzyme-free electrochemical sensor based on a rod-shaped bimetallic MOF anchored on graphene oxide nanosheets for determination of glucose in Huangshui. *Anal. methods Adv. methods Appl.* 15 (20), 2417–2426. doi:10.1039/d2ay01977a
- Mallakpour, S., Nikkhou, E., and Hussain, C. M. (2022). Application of MOF materials as drug delivery systems for cancer therapy and dermal treatment. *Coord. Chem. Rev.* 451, 214262. doi:10.1016/j.ccr.2021.214262
- McBride, J. A., Carson, C. C., and Coward, R. M. (2018). The availability and acquisition of illicit anabolic androgenic steroids and testosterone preparations on the internet. *Am. J. men's health* 12 (5), 1352–1357. doi:10.1177/1557988316648704
- Mehmandoust, M., Erk, E. E., Soylak, M., Erk, N., and Karimi, F. (2022). Metal-organic framework based electrochemical immunosensor for label-free detection of glial fibrillary acidic protein as a biomarker. *Industrial and Eng. Chem. Res.* 62 (11), 4532–4539. doi:10.1021/acs.iecr.2c01445
- Mohamad, N. V., Soelaiman, I. N., and Chin, K. Y. (2016). A concise review of testosterone and bone health. *Clin. interventions aging* 11, 1317–1324. doi:10.2147/CLIA.S115472
- Moura, S. L., de Moraes, R. R., dos Santos, M. A. P., Pividori, M. I., Lopes, J. A. D., Moreira, D. L., et al. (2014). Electrochemical detection *in vitro* and electron transfer mechanism of testosterone using a modified electrode with a cobalt oxide film. *Sensors Actuators B Chem.* 202, 469–474. doi:10.1016/j.snb.2014.05.104
- Naseri, M., Pitzalis, F., Carucci, C., Medda, L., Fotouhi, L., Magner, E., et al. (2018). Lipase and laccase encapsulated on zeolite imidazolate framework: enzyme activity and stability from voltammetric measurements. *Chem. Cat. Chem.* 10 (23), 5425–5433. doi:10.1002/cctc.201801293
- Pérez, O., Odio, O. F., and Reguera, E. (2022). XPS as a probe for the bonding nature in metal acetates. *New J. Chem.* 46, 11255–11265. doi:10.1039/D2NJ01905A
- Rojas-Guerrero, C. A., Villanueva-Rodríguez, M., Guzmán-Mar, J. L., Hernández-Ramírez, A., Cedillo-González, E. I., Longoria Rodríguez, F. E., et al. (2023). Solar photocatalytic degradation of polyethylene terephthalate nanoplastics: evaluation of the applicability of the TiO<sub>2</sub>/MIL-100(Fe) composite material. *J. Environ. Chem. Eng.* 11. doi:10.1016/j.jece.2023.110415
- Roth Stefaniak, K., Epley, C. C., Novak, J. J., McAndrew, M. L., Cornhill, H. D., Zhu, J., et al. (2018). Photo-triggered release of 5-fluorouracil from a MOF drug delivery vehicle. *Chem. Commun.* 54 (55), 7617–7620. doi:10.1039/c8cc01601a
- Sánchez-Almirola, J., Gage, A., Lopez, R., Yapell, D., Mujawar, M., Kamat, V., et al. (2023). Label and bio-active free electrochemical detection of testosterone hormone using MIP-based sensing platform. *Mater. Sci. Eng. B* 296, 116670. doi:10.1016/j.mseb.2023.116670
- Sánchez-Sánchez, M., Getachew, N., Díaz, K., Díaz-García, M., Chebudeb, Y., and Díaz, I. (2015). Synthesis of metal-organic frameworks in water at room temperature: salts as linker sources. *Green Chem.* 17, 1500–1509. doi:10.1039/C4GC01861C

- Sanli, S., Moulahoum, H., Ghorbanizamani, F., Gumus, Z. P., and Timur, S. (2020). On-site testosterone biosensing for doping detection: electrochemical immunosensing via functionalized magnetic nanoparticles and screen-printed electrodes. *ChemistrySelect* 5, 14911–14916. doi:10.1002/slct.202004204
- Savan, E. K. (2020). Square wave voltammetric (SWV) determination of quercetin in tea samples at a single-walled carbon nanotube (SWCNT) modified glassy carbon electrode (GCE). *Anal. Lett.* 53, 858–872. doi:10.1080/00032719.2019.1684514
- Scovell, J. M., Ramasamy, R., Wilken, N., Kovac, J. R., and Lipshultz, L. I. (2015). Hypogonadal symptoms in young men are associated with a serum total testosterone threshold of 400 ng/dL. *BJU Int.* 116 (1), 142–146. doi:10.1111/bju.12970
- Serafin, V., Eguilaz, M., Agui, L., Yáñez-Sedeño, P., and Pingarrón, J. M. (2011). An electrochemical immunosensor for testosterone using gold nanoparticles – carbon nanotubes composite electrodes. *Electroanalysis* 23, 169–176. doi:10.1002/elan.201000419
- Tortolini, C., Cass, A. E. G., Pofi, R., Lenzi, A., and Antiochia, R. (2022). Microneedle-based nanoporous gold electrochemical sensor for real-time catecholamine detection. *Microchim. Acta* 189 (180), 180. doi:10.1007/s00604-022-05260-2
- Tortolini, C., Gigli, V., Angeloni, A., Isidori, A., and Antiochia, R. (2024a). Simple and sensitive voltammetric sensor for *in-situ* clinical and environmental 17- $\beta$ -estradiol monitoring. *Electroanalysis* 36, e202300417. doi:10.1002/elan.202300417
- Tortolini, C., Gigli, V., Angeloni, A., Tasca, F., Thanh, N. T. K., and Antiochia, R. (2024b). A disposable immunosensor for the detection of salivary MMP-8 as biomarker of periodontitis. *Bioelectrochemistry* 156, 108590. doi:10.1016/j.bioelechem.2023.108590
- Tyszczuk, K. (2008). Application of an *in situ* plated lead film electrode to the analysis of testosterone by adsorptive stripping voltammetry. *Anal. Bioanal. Chem.* 390, 1951–1956. doi:10.1007/s00216-008-1928-9
- Wang, C., and Liao, K. (2021). Recent advances in emerging metal- and covalent-organic frameworks for enzyme encapsulation. *ACS Appl. Mater. and interfaces* 13 (48), 56752–56776. doi:10.1021/acsami.1c13408
- Wang, C., Zhang, X., Liu, Y., Li, J., Zhu, L., Lu, Y., et al. (2022). An enzyme-particle hybrid ink for one step screen-printing and long-term metabolism monitoring. *Anal. Chim. acta* 1221, 340168. doi:10.1016/j.aca.2022.340168
- Xu, Q.-Y., Tan, Z., Liao, X.-Y., and Wang, C. (2022). Recent advances in nanoscale metal-organic frameworks biosensors for detection of biomarkers. *Chin. Chem. Lett.* 33 (1), 22–32. doi:10.1016/j.ccllet.2021.06.015
- Yadav, R., Yadav, N., and Kharya, M. D. (2014). Steroid chemistry and steroid hormone action: a review. *Asian J. Res. Chem.* 7 (11), 964–969.
- Yadav, S. K., Chandra, P., Goyal, R. N., and Shim, Y. B. (2013). A review on determination of steroids in biological samples exploiting nanobio-electroanalytical methods. *Anal. Chim. acta.* 762, 14–24. doi:10.1016/j.aca.2012.11.037
- Yuki, A., Otsuka, R., Kozakai, R., Kitamura, I., Okura, T., Ando, F., et al. (2013). Relationship between low free testosterone levels and loss of muscle mass. *Sci. Rep.* 3, 1818. doi:10.1038/srep01818
- Zhao, J., Zhang, Y., Luo, Y., Zheng, W., Xu, X., and Luo, F. (2024). Amorphous metal-organic frameworks: pioneering frontiers in cancer diagnostics and therapeutics. *Chem. Eng. J.* 492, 152295. doi:10.1016/j.cej.2024.152295